Single crystal growth by the Bridgman-Stockbarger technique of CaF2-rich - TmF3 solid solutions: Evidence of mixed valence Tm2+ and Tm3+ cations

Gabriel Buse, Carla Schornig, Marius Stef, Maria Poienar, Dragos Tatomirescu, Alexandra Popescu, Jérôme Debray, Vincent Motto-Ros, Frédéric Pelascini, Daniel Vizman, et al.

Journal of Alloys and Compounds 1010 (2025) 177784

Contents lists available at ScienceDirect

Journal of Alloys and Compounds

journal homepage: www.elsevier.com/locate/jalcom

Single crystal growth by the Bridgman-Stockbarger technique of CaF_2-rich - TmF_3 solid solutions: Evidence of mixed valence Tm^{2+} and Tm^{3+} cations

Gabriel Buse [a], Carla Schornig [b], Marius Stef [b], Maria Poienar [a], Dragos Tatomirescu [b], Alexandra Popescu [b], Jérôme Debray [c,d], Vincent Motto-Ros [e], Frédéric Pelascini [f], Daniel Vizman [b], Philippe Veber [a,b,*]

[a] West University of Timisoara, Institute for Advanced Environmental Research, ICAM, 4 Strada Oituz, Timișoara, Romania
[b] West University of Timisoara, Faculty of Physics, Crystal Growth Laboratory, 4 Bd Vasile Parvan, Timișoara 300223, Romania
[c] Université Grenoble Alpes, Institut Néel, Grenoble F-38042, France
[d] CNRS, Institut Néel, Grenoble F-38042, France
[e] Université Lyon, Université Claude Bernard Lyon 1, CNRS, Institut Lumière Matière, UMR 5306, Villeurbanne F-69100, France
[f] CETIM, 67400, Illkirch Graffenstaden, France

ARTICLE INFO

Keywords:
Fluorides
Single crystals
Bridgman technique
Numerical modelling
Elemental segregation
Spectroscopic analysis

ABSTRACT

Crystal growth and numerical simulation of CaF_2-rich-based solid solution with TmF_3 have been performed by the Bridgman-Stockbarger technique with initial Tm content 0.1 mol%, 1 mol% and 5 mol%. Centimeter-sized single crystals were obtained. Growth in the vicinity of (110) and (210) crystallographic directions have been identified as the natural crystal habit for the CaF_2-rich- TmF_3 solid solution with an axial thermal gradient about $G=12\ K.cm^{-1}$ and a pulling rate of $v=4\ mm.h^{-1}$. Optical absorption spectroscopy evidenced the presence of both Tm^{2+} and Tm^{3+} cations within the matrix. Their respective effective partition coefficients $k_{eff}(Tm^{2+})$ and $k_{eff}(Tm^{3+})$, close to unity, have been calculated. For low TmF_3 initial content, with 0.1 mol.% and 1 mol.%, $k_{eff}(Tm^{2+})>1$ and $k_{eff}(Tm^{3+})>1$ whereas $k_{eff}(Tm^{2+})<1$ and $k_{eff}(Tm^{3+})<1$ for the attempt with 5 mol% TmF_3 initial content. For this latter, a global effective partition coefficient, including both Tm^{3+} and Tm^{2+} contents, is logically deduced to be $k_{eff}([Tm])<1$. Chemical analysis carried out by ICP-AES and LIBS confirmed this trend with an effective partition coefficient of the global [Tm] content in the crystal that can be lower than 1. The global estimated partition coefficient of [Tm] in CaF_2 matrix is thus ranging in between 0.906 and below 1 for 5 mol.% TmF_3 molar fraction. The expected congruent melting point in the CaF_2-rich-region of the CaF_2-TmF_3 phase diagram is evidenced and is higher than 1 mol.% and below 5 mol.% TmF_3 molar fraction. Finally, carbon environment and TmF_3 synproportionation reaction are pointed out as the main likely causes of Tm^{3+} cation reduction into Tm^{2+} during the growth process.

1. Introduction

Fluoride-based materials are well known [1] due to their intrinsic properties, such as a high optical transparency (VUV–VIS–IR range), low phonon energy, small refractive index, remarkable physicochemical properties (non-hygroscopy in most cases) and ease of machining and polishing. In addition, they have great ability to host various doping-cations with 3d or 4 f electronic configuration. Owing to their specific features, fluoride-based single crystals exhibit enhanced properties, which are of particular interest in numerous physical phenomena ranging from luminescence, scintillation and up-conversion to solid-state laser effect. A wide range of fluoride matrix have been investigated through time such as CaF_2, BaF_2 or CeF_3 [1–4] and many others such as: TbF_3, $LiYF_4$ (LYF), $LiTbF_4$, KYF_4, $LiLuF_4$ (LuLiF), KY_3F_{10} (KYF), KTb_3F_{10} (KTF), BaY_2F_8, $LiCaAlF_6$ (LiCAF), $LiSrAlF_6$ (LISAF), $KMgF_3$ (KMF), $BaLiF_3$, $KAlF_4$, $Na_5Al_3F_{14}$ [1,5–13]. When doped with suitable cations, fluoride compositions open up opportunities in many application fields such as window materials, tunable lasers, defence, telecommunication, optical lenses or remote sensing. Crystal growth of bulk fluorides are mainly carried out by the Czochralski technique [1,12,14], Bridgman technique in a slightly lower extent [9,15], and seldom by Top Seeded Solution Growth [6,16] or micro-pulling down technique

* Corresponding author at: West University of Timisoara, Institute for Advanced Environmental Research, ICAM, 4 Strada Oituz, Timișoara, Romania.
E-mail address: philippe.veber@e-uvt.ro (P. Veber).

https://doi.org/10.1016/j.jallcom.2024.177784
Received 3 September 2024; Received in revised form 7 November 2024; Accepted 25 November 2024
Available online 26 November 2024

[17]. In particular, Bridgman technique features particular advantages by comparison with the other techniques. Indeed, it enables the setting of an accurate thermal profile in both liquid and solid phases for a steady controlled growth and homogeneous cooling-down of as-grown boules. It also enables the control of the atmosphere in order to perform single crystal growth with stoichiometric compositions, low amount of ionic vacancies, low oxygen pollution and no hydroxyl substitution.

Because rare-Earth ions are attractive for achieving optical applications in the visible, near and mid-infrared spectral range, in the following, Tm doping cation is considered in order to perform high quality Tm^{3+}-doped CaF_2 single crystal growth. Tm^{3+} is a very interesting doping cation [12,18–20] because of its electronic configuration, which allows several optical emission at 1.5μm, 1.9μm and 2.3μm. Hence, Tm^{3+}-doped fluoride single crystals are promising for the realization of eye-safe laser, remote sensing of atmospheric species such as CH_4, infrared counter-measurements or for medicine purposes. However, as previously reported [21], CaF_2 doped with TmF_3 exhibit both Tm^{3+} and Tm^{2+} cations. In the present work, we report the crystal growth, the numerical modelling and the characterization on the chemical behaviour of TmF_3 in single crystalline CaF_2 solid solutions obtained by the Bridgman-Stockbarger method. That aims at clarifying the origin of the Tm^{3+} reduction into Tm^{2+} through their respective chemical distribution and segregation. Three initial TmF_3 contents were assessed: 0.1 mol.%, 1 mol.% and 5 mol.% in order to screen the CaF_2-rich region of CaF_2-TmF_3 phase diagram where the most interesting compositions for the above-mentioned optical applications are found. Structural study and crystal habit characterized by Laue experiments enable to identify preferential growth directions in the as-grown crystals. Optical absorption characterization of the crystals is displayed leading to the evidence of mixed valence of Tm^{3+} and Tm^{2+} cations within the CaF_2 matrix. LIBS coupled to ICP-AES analysis and optical measurements enable to characterize, respectively, the chemical homogeneity and optical absorption of the boules at different stages of the growth. Effective partition coefficients of thulium are calculated by these two methods and are discussed with respect to the CaF_2-TmF_3 phase diagram.

2. Experimental procedure

2.1. Crystal growth

CaF_2-rich solid-solution single crystals doped with initial 0.1 mol.%, 1 mol.% and 5 mol.% TmF_3 contents were grown by using the vertical Bridgman-Stockbarger method [3]. Crushed and sieved pure CaF_2 optical UV–VIS crystals from Crystran Ltd. UK and commercial powder from Alfa Aesar of TmF_3 with 99,999 % (5 N) purity were chosen as raw materials. Raw materials were mixed and inserted thoroughly in a 10-cm long and 1-cm wide graphite crucible without prior synthesis. Graphite is used because carbon cannot react with CaF_2 and TmF_3 and its wettability is virtually zero with respect to liquid fluorides [22], making easy to extract boules without them sticking to the inner surface of the crucible. The crucible, after closing with a graphite screw-on cap at its top, is set in the furnace. The solid solution is synthesized and melted when the CaF_2-TmF_3 mixture is heated up in 5 hours, under a 5×10^{-5} torr vacuum atmosphere, above the melting point of CaF_2 with a maximum temperature of 1785 K. The melt is soaked during 3 hours then pulled down with v=4 $mm.h^{-1}$ translation speed. Prior to the growth, a longitudinal temperature distribution along the axis of the furnace was measured with a S-type thermocouple and a thermal gradient about G=12 $K.cm^{-1}$ was achieved in the adiabatic zone where the solid-liquid interface stands. Once the crucible was translated over all its length within the furnace, the translation is stopped and the furnace is cooled down within 24 h. The as-grown crystals are then cleaved [23] with a hammer and a metallic blade into 10–30 ellipsoidal-like-shaped slices of ~1.5–3 mm thickness along the well-known (111) directions [23,24]. As-cleaved slices are hereinafter used for optical, chemical and structure characterization.

2.2. Numerical modelling

CrysMAS code is a finite-volume numerical tool developed by the Crystal Growth Laboratory within the Fraunhofer Institute of Integrated Systems and Device Technology (IISB) at Erlangen in Germany [25–27] and was used for the numerical modelling of the crystal growth experiment. It allows simulating heat transfer, fluid flow and solid–liquid interface shape during crystallization with respect to latent heat, radiative transport, and conduction and convection heat phenomena. The features of the furnace are described in our previous work [3] and were schematized via a 2D-Computer-Aided-Design-like tool integrated to the software. The global geometry of the furnace is presented in Fig. 1a. The temperature gradient in the ampoule is generated by a shaped graphite heater. The thermokinetic parameters of the materials constituting the Bridgman device are listed in Table 1.

Inverse 2D-axisymmetric global simulations were performed in order to determine the thermal gradient in the furnace. For this, a control point placed at the symmetry axis at a height of 18.5 cm from the heather bottom, where the temperature of 1688 K was measured in experiment. This, in turn was adapted for local simulation of the crucible. The heat transfer mechanisms that are considered during the simulations are conduction, convection and radiative heat transfer. For this study, the main goal of the numerical simulation was to evaluate the level of convection and consequently the melt mixing in different stages of the crystal growth. Therefore, in order to save computational time, a local numerical model was considered consisting of an axisymmetric graphite crucible with an inner diameter of 10 mm and an outer graphite wall with a thickness of 2 mm placed in the temperature gradient obtained from global simulation (Fig. 1b). At the bottom of the crucible, the geometry contains a tip with a maximum diameter of 2 mm and a height of 4 mm. From this point, the crystal thickness gradually increases until it reaches a final crystal radius of 5 mm. A 1 mm thick graphite floater is placed 58 mm from the tip of the crucible similarly with the experimental set-up. The floater is designed to prevent excessive volatilization of the liquid solution in the upper part of the crucible where the temperature is the highest. The floater is always in contact with the liquid phase at any stage of the growth and it is almost liquid-tight near the inner wall of the graphite crucible. Moreover, previous simulations have shown that the addition of the floater has no significant influence at the beginning of the growth. Its influence is efficient when the solidified fraction (fs) approaches fs=1, so that the floater acts as a thermal shield and prevents, at the end of the growth, a too high cooling rate at the free surface level. The solid-liquid interface is assumed to be present on the melting point isotherm, where latent heat is released due to the solidification process. CrysMAS uses the well-established Gebhart view factors to describe the ratio of radiation absorbed by any other surface versus the total emitted radiation from given surface and the n-Band model for treatment of the spectral behaviours. which was proven to produce accurate results with relatively low computational cost [36, 37]. Note that the material is totally transparent only in the defined spectral bands and is totally opaque in the rest of the spectrum.

Four stages of crystal growth were considered, as follows: C0 – fs = 0; C1 – fs = 0.25; C2 – fs = 0.52; C3 – fs = 0.86 (where fs indicates the solidified fraction) and the temperature distribution is studied. The temperature profile obtained from global simulation was used as boundary conditions for the lateral side of the crucible. For the top and bottom boundaries of the crucible, we used fixed temperature values. At the melt-crucible interface a zero-velocity boundary condition was imposed. The physical properties for the materials used in the numerical modelling are listed in Table 1 and are assumed to be constant with temperature (if not specified otherwise). Grid refinement and time steps used in these computations were tested to ensure accurate results.

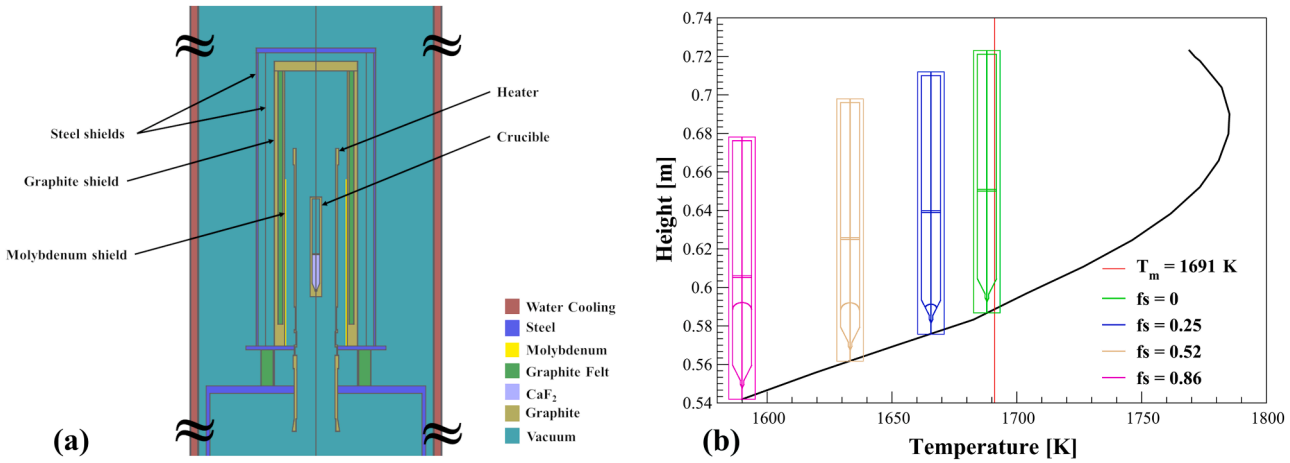

Fig. 1. (a) Furnace and ampoule geometry. (b) Temperature gradient and four crucible positions for different solidification fraction. The black line represents the longitudinal distribution of the temperature with respect to the position (height) of the crucible in the furnace.

Table 1
Thermo-physical parameters used for modelling with CrysMAS code.

Description	Value	Reference
CaF_2 crystal		
Density (kg•m^{-3})	3200	[28]
Thermal Conductivity (W•m^{-1}•K^{-1})	9.71	[29]
Specific heat capacity (J•kg^{-1}•K^{-1})	766.3 + 0.39•T + 2.52×10^5•T^{-2}	[30]
Visibility bands (μm)	0.15 – 9	[31]
Melting temperature (K)	1691	[31]
Refraction index	1.43	[28]
Thermal expansion (K^{-1})	1.87×10^{-5}	[28]
CaF_2 melt		
Density (kg•m^{-3})	3767–0.694•T	[32]
Thermal Conductivity (W•m^{-1}•K^{-1})	0.6	[28]
Specific heat capacity (J•kg^{-1}•K^{-1})	1280	[33]
Latent heat (J•kg^{-1})	320000	[28]
Visibility bands (μm)	0.15–9	[31]
Refraction index	1.43	[28]
Viscosity (kg•m^{-1}•s^{-1})	0.000371205•exp(2470•T^{-1})	[34]
Volumetric expansion (K^{-1})	0.0002682	[35]
Graphite		
Thermal Conductivity (W•m^{-1}•K^{-1})	115.74–0.0982•T + 3.61×10^{-5}•T^2 - 4.29×10^{-9}•T^2	[28]
Emissivity	0.8	[28]
Molybdenum		
Thermal Conductivity (W•m^{-1}•K^{-1})	163.7–0.062•T + 9.72×10^{-6}•T^2	[28]
Emissivity	0.4	[28]

2.3. Chemical and physical analysis

Powders resulting from crushed single crystals and a 63-μm sieving were analysed by X-Ray Diffraction (XRD). XRD patterns were collected on a Bragg-Brentano θ-θ geometry diffractometer Bruker D8 Advance working with Cu anticathode (40 kV, 40 mA), 0.3° slits and Ni filter. The data were collected over an angular range of 2θ = 5°-90° with a 0.006° step. XRD patterns were studied using the known space groups Fm-3m of CaF_2 [38]. Lattice parameters were refined by Rietveld method using the FullProf [39] software. Laue back-scattering patterns were recorded using a Photonic Science CCD camera by averaging of 6 images snapped for 1 minute. A stationary crystal is irradiated with a 0.7-mm collimated polychromatic X-ray beam supplied by a tungsten anticathode working at 35 kV and 40 mA (Seifert ID3003 generator). The polished samples were held on a goniometric head and set perpendicular to the X-ray beam using an autocollimator. OrientExpress software [40] was used for pattern indexing, with an orientation accuracy is of 0.5°.

Thulium elemental content measurements were performed by using Inductively Coupled Plasma - Atomic Emission Spectroscopy (ICP-AES) using the Vista MPX (Varian). For the analysis, samples containing a mixture of calcium fluoride (CaF_2) and thulium (Tm) were quantified at three designated concentration levels. Samples were weighed accordingly: ranging from 50.6 mg to 98.6 mg, to align with the predetermined concentrations. These samples underwent a controlled digestion process in a 1:1 hydrochloric acid solution within 50 mL digestion tubes, which involved sequential heating at 383 K for one hour, 393 K for 1.5 hours, and 413 K for four hours. After cooling, the digested samples were transferred to volumetric flasks and diluted to a final volume of 60 microliters with filtered water on the following day. The standard addition method was applied to counteract matrix effects, utilizing a thulium standard solution (1000 mg.l^{-1} in 2–3 % nitric acid, Supelco reference 1.70361.0100, Merck/Aldrich) that was appropriately diluted. The calibration involved systematically increasing the volume of the standard solution added to a constant volume of the sample mixture, with adjustments in the volume of water to maintain consistent total volumes across all test solutions. This meticulous approach enabled precise calibration essential for accurate quantification.

The Varian Vista MPX ICP-AES was employed to measure thulium concentrations, focusing on its spectral lines at 313.125 nm and 336.261 nm. The instrument settings were optimized to achieve accurate detection and quantification limits specific to thulium's spectral characteristics. The results of the analysis are listed in Table 2. Additionally, a recovery test on the standard solution showed no significant loss, with a recovery rate of 104.54 %. This confirms the high accuracy and reliability of the method, demonstrating effective compensation for potential analytical deviations and ensuring the integrity of the thulium quantification in these complex sample matrices.

LIBS-based imaging setup [41–44] was used to image the distribution of Ca, F and Tm in the different sections of as-grown crystal growth slices. A Nd:YAG laser (Centurion GRM, Lumibird) was used with 7 ns

Table 2
Tm content measured by ICP-AES for the different growth attempts.

Attempt	Wgh.% Tm	Wgh.% Tm accuracy	Mol.% Tm	Mol.% Tm accuracy
5 mol.% Tm-doped CaF_2	9.74 %	1.09 %	4.92 %	0.60 %
1 mol.% Tm-doped CaF_2	1.97 %	0.07 %	0.93 %	0.03 %
0.1 mol.% Tm-doped CaF_2	0.243 %	0.012 %	0.1126 %	0.0060 %

pulse duration and 100 Hz repetition rate, emitting at the fundamental wavelength (1064 nm). A x15 magnification objective microscope (LMM-15X-P01, Thorlabs) was used to focus the laser beam onto the sample surface). An energy of 1 mJ was set for all the acquisition, with an argon flow directed to the plasma region of 0.8 $l.min^{-1}$ to prevent surface contamination by ablated material redeposition of the previous laser shots and to improve the sensitivity due to better plasma confinement. The experiment was done at room temperature and ambient pressure. During the analysis, the sample surface was scanned, through single laser pulses, in a pixel-by-pixel manner inducing the breakdown and sparks of the material. The light radiation emitted by the plasma was collected by an optical system and analysed using a spectrometer (Shamrock 500, Andor technology) equipped with an intensified charge-coupled device (ICCD) camera (istar, Andor technology). The spectrometer was configured in the spectral range from 345 nm to 385 nm (1200 $l.mm^{-1}$ grating) in order to detect both Ca and Tm lines (see Fig. 1 in supplementary material). In this configuration, the spectral resolution was 0.08 nm. The ICCD camera was synchronized to the Q-switch of the laser. A gain of 500 was applied, with a delay and a gate width of 0.5 μs and 5 μs, respectively. For the shown LIBS imaging results, the step size between each laser shot was fixed to 40 μm.

The intensity calibration was performed with respect to the 3 above mentioned reference samples analysed with ICP-AES. For these 3 samples, LIBS imaging was obviously carried out before sample dissolution required for ICP-AES analysis. For these 3 analyses, a mask was defined by removing the influence of the edges of the crystal sections which could be affected by de sample preparation. These masks were produced from the calcium images. An average LIBS spectrum was then determined for each section (i.e. average of all spectra contained in the mask). Assuming that the concentration of Tm was homogeneous in volume (i.e. correspondence between LIBS surface analysis and ICP-AES volume analysis), we built a quantitative model by plotting the LIBS intensity of Tm as a function of the concentration obtained with ICP-AES. A special attention was paid to the choice of the Tm line. Indeed, given the concentration range of interest (up to 10 % molar), the intense Tm lines observed on the spectrum suffered from self-absorption, resulting in a non-linear quantitative model. We, therefore, turned our attention to the line at 383.8 nm, which is weak but unaffected by these saturation phenomena (see resulting model on Fig. 2 in supplementary material). A very good linearity is obtained, with a coefficient of determination of 0.9993. With the evaluation of the confidence hyperbola, we were able to estimate the associated LIBS uncertainties at around 3.7 % for a 5 % Tm molar concentration, 10 % for 1 mol.%Tm, and 100 % for a 0.1 mol.%Tm.

Finally, to investigate the distribution of both Tm^{3+} and Tm^{2+} cations along CaF_2 crystal lengths and to calculate the effective segregation coefficient, the optical absorption method was used as previously described [45,46]. The optical absorption spectrum of each slice was measured, at room temperature, in UV–VIS spectral range using a Shimadzu 1650PC spectrophotometer.

3. Results and discussion

3.1. Numerical modelling

The main parameters that influence the solid-liquid (S-L) interface shape in a crystal grown by the Bridgman technique are the growth rate and the temperature gradient. The radiative heat transfer will also affect the shape of the S-L interface, therefore we have set both the melt and crystal CaF_2 as semi-transparent materials (transparent between 0.15 – 9 μm). We investigated the convection patterns of the melt and interface shape under different solidified fractions (fs) and temperature gradients during CaF_2 growth using pseudostationary numerical simulations. In Fig. 2, we can see, respectively, axial and radial velocity distribution.

In general, the Bridgman configuration is hydrodynamically stable due to the temperature gradient (hot melt is in the upper part and cold melt is in the lower part of the crucible). When the growth starts, the deflection of the S-L interface generates radial temperature gradients, which in turn generates a stronger melt convection. From Fig. 2a. we can observe that there is a difference of two orders of magnitude between the maximum velocity in the cone and the maximum velocity in the cylindrical part of the crucible. The small velocities in the tip of the crucible ($\sim 10^{-7}$ $m.s^{-1}$) lead to a poor mixing of the melt in the early stages of the crystallization process. This may be caused by the vortex that forms near

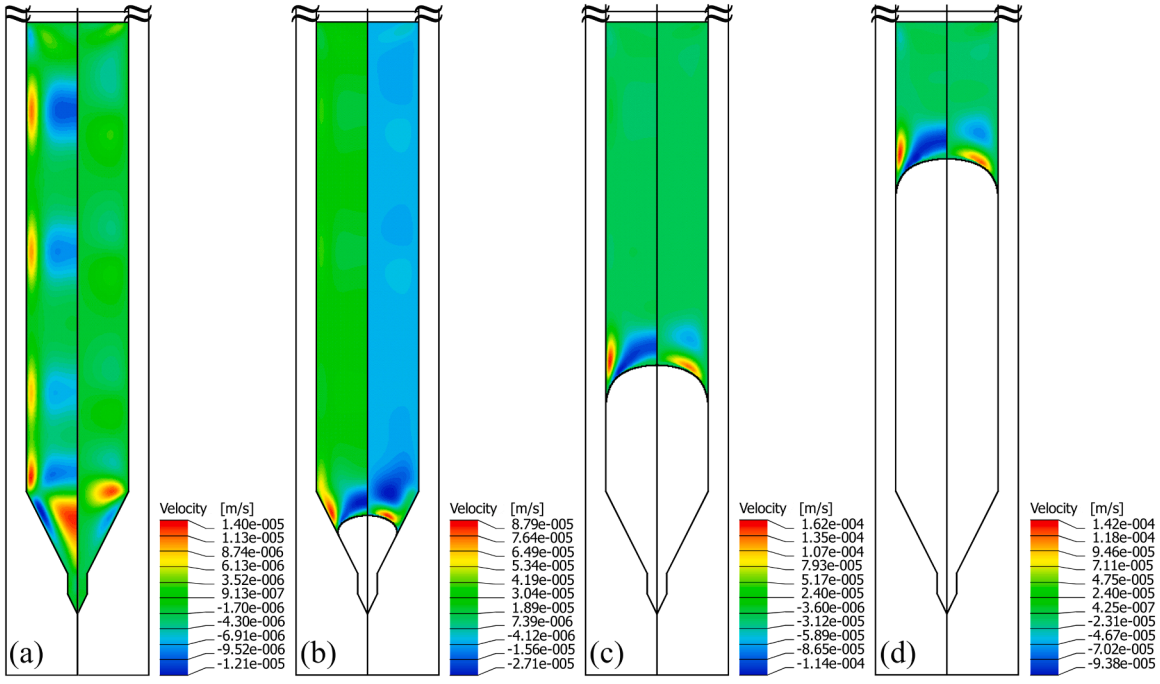

Fig. 2. Velocity field distribution along the axial (left side) and radial (right side) directions for different solidified fractions: (a) C0 – fs = 0, (b) C1 – fs = 0.25, (c) C2 – fs = 0.52 and (d) C3 – fs = 0.86.

the crucible shoulder, at the end of the conical part that does not reach the tip of the crucible and is unable to mix the melt in the tip with the rest of the melt. As for the crystallization front near the end of the conical part and further out (for fs>0.25, Fig. 2b, c and d), the velocities in the vortex generated near the S-L interface becomes one order of magnitude higher than in the start phase (Fig. 2a.). This vortex ensures a much better mixing in the melt in comparison with the start phase.

Interface deflection is defined as the perpendicular distance between the centre point of the S-L interface and the point where the melt, the crystal and the crucible come into contact. The evolution of the S-L interface can be seen in Fig. 3. The numerical results show that the interface presents a convex shape throughout the whole growth process. In the cylindrical region of the crucible, the convexity of the S-L interface (defined as the ratio between the maximum interface deflection and the crystal width) decreases from 0.73 (C2) to 0.68 (C3) due to the increase in crystal size that leads to a higher latent heat released during the solidification process.

3.2. Crystal growth

Centimetre-sized as-grown boules were obtained (Fig. 4) with lengths up to 90 mm and 10 mm in diameter. A thin graphite layer is observed at the outer surface of the as-grown boules. As shown by the numerical modelling (Fig. 3), a convex solid-liquid interface is observed during the whole growth process. This result is consistent with what was observed with BaF_2, as an isotype of CaF_2, boules and growth simulations in the same conditions [47,48]. Since carbon cannot enter the CaF_2 matrix, radial growth occurred from the centre of the liquid towards the graphite wall of the crucible enabling the graphite impurities contained in the liquid to be rejected towards the periphery of the growing boule, leaving the core of the boule free of inclusions. However, few macroscopic black carbon inclusions at the late end of the boules are detected. We assume that because of the poor intrinsic late-end-of-growth conditions of Bridgman technique, the carbon impurities contained in the final part of the solidifying liquid are inevitably trapped. After graphite removal from the outer surface, the boules display homogenously clear regions in their entire volume (Fig. 5) without macroscopic inclusions visible with a binocular under magnification X64.

3.3. XRD and Laue characterization

The X-ray diffraction patterns (Fig. 6) collected on crushed single crystals for 0.1 mol.%, 1 mol.% and 5 mol.% TmF_3-doped CaF_2 samples at several stages of the growth feature a typical crystallized fluorite structure with Fm-3m space group. No secondary phases were detected. Calculated lattice parameters are mentioned in Table 3 along with those reported in the literature for undoped CaF_2 samples [49]. The refined

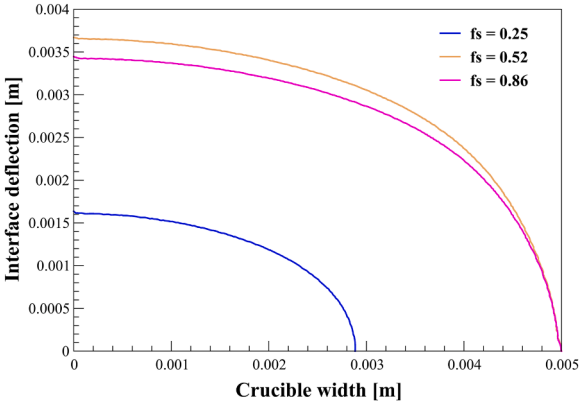

Fig. 3. Evolution of the S-L interface deflection during the growth process from numerical simulation.

parameters for our samples are in agreement with those previously reported for the fluorite structure [49], with slightly increased unit cell parameters/volume values due to the Tm doping into the CaF_2 matrix. Moreover, the cell volume slightly increases from 163.189(8) $Å^3$ (0.1 mol%TmF_3-doped CaF_2 sample) to 163.768(3) $Å^3$ (5 mol.% TmF_3-doped CaF_2 sample), pointing out the enrichment of Tm cations in Ca sites and fluorine anions in interstitial sites of the cubic CaF_2 crystal structure. Lattice parameters calculated (Table 3) from Rietveld measurements were used for Laue experiments.

Natural crystallographic cleavage plane (111) was confirmed by Laue X-ray diffraction (Fig. 7a). Laue characterization of the boules has shown polycrystalline bulk in the 4-mm long seed location up to the beginning of the 5-mm long cone height. However, one single grain, overall the cross section of the crucible, is invariably detected for the 3 growth attempts from the end of the conical part. As no seed was used during the growth, numerous grains spontaneously nucleated in the seed location. These grains grew in the conical part until one remaining single grain was naturally selected. Growth attempts along this selected natural crystallographic direction enabled the growth of one single crystal from the end of the conical part and in the whole cylindrical volume of the crucible.

With respect to the thermokinetic parameters used in the Bridgman furnace of the present work (see paragraph 2), the natural growth directions of the as-grown crystals have been identified to be in the vicinity of the (110) crystallographic direction, where dense in-plane Ca-F chemical bonds are located, and (210) crystallographic direction. That is consistent with what was previously reported by Senguttuvan *et al.* [50] for CaF_2 Bridgman growth by spontaneous nucleation with similar thermokinetic parameters, where a longitudinal gradient about G=10 K.cm^{-1} and growth velocity about v=1 mm.h^{-1} were used. (Fig. 7b and c). In addition, crystal habit, which refers to the crystal shape and natural crystallographic growth plans with respect to its structure and growth conditions, is strongly supported by the observed stability of the present growth attempts. Indeed, according to the Tiller criterion G/v [51] related to Mullins-Sekerka morphological instabilities [52,53], Fedorov *et al.* [54] calculated that Tiller criterion for the stable Bridgman growth of CaF_2, with a low amount of SrF_2 impurities, must be G/v>1.88×10^4 K.s.cm^{-2} in order to avoid morphological instabilities and constitutional supercooling. In the present work, as well as in the work of Senguttuvan *et al.* [50], G/v is calculated to be, respectively, G/v= 1.08 ×10^5 K.s.cm^{-2} and G/v= 3.60 ×10^5 K.s.cm^{-2}. They are greatly higher than the limit given by Fedorov *et al.* [54] enabling thus the habit of the crystal to develop naturally along these crystallographic directions with respect to the thermokinetic conditions employed. Finally, for each growth attempt, geometrical angles in between as-cleaved plan and growth direction were measured around 40°±5° and are consistent with theoretical calculated values of 35.26° and 39.23° in between (111) and, respectively, (110) and (210) directions for CaF_2 cubic structure.

3.4. Effective partition coefficients calculated from chemical and optical measurements

The effective partition coefficient k_{eff} is defined by $k_{eff}= C_S / C_L^0$, where C_L^0 is the dopant concentration in the initial melt and C_S is the dopant concentration at the early beginning of the as-grown crystal. The value of C_S can be measured by various methods, from chemical analysis to optical absorption measurements [55–60].

3.4.1. Chemical analysis

Several slices extracted from the seed location, the conical and the cylindrical parts were analysed by LIBS and ICP-AES. The average concentration of Tm molar content in each slice is calculated from every point of the LIBS mapping overall the whole sample surface. Note that the global content of [Tm] in the crystal measured by this method includes both Tm^{2+} and Tm^{3+} contents since these two cations cannot be distinguished with LIBS technique.

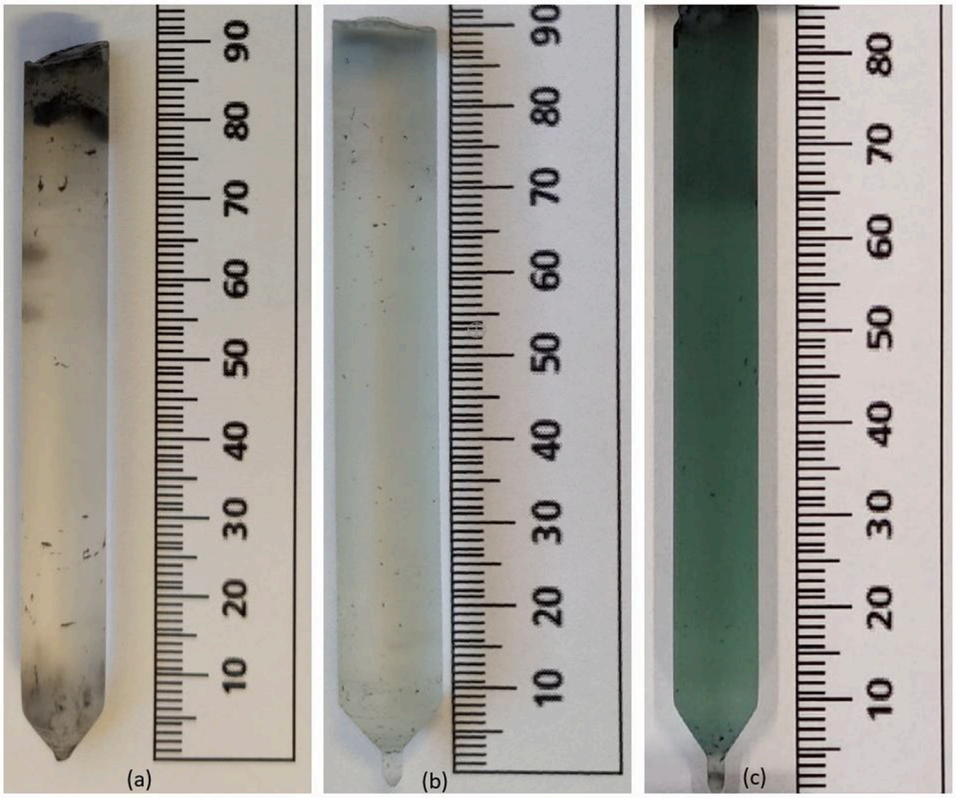

Fig. 4. (a) 0.1 mol.% Tm-doped CaF_2 as-grown single crystal; (b) 1 mol.% Tm-doped CaF_2 as-grown single crystal; and (c) 5 mol.% Tm-doped CaF_2 as-grown single crystal.

Fig. 5. Example of cleaved defect-free slices, numbered from n°1 to n°24, obtained all along the growth axis for 1 mol.%Tm-doped CaF_2 single crystal. The thickness of each slice is indicated below the number of the slice. No change in colour is observed in all the slices.

On the one hand, we consider (111)-orientated slices extracted from the cylindrical part. LIBS imaging revealed a highly homogeneous distribution of the dopant content on the whole surface of the 9 analysed slices (Fig. 8). In particular, no Tm radial segregation is detected. As shown in Fig. 3, a strong convex S-L interface occurs during the whole growth process, meaning that the crystallization occurs from the centre towards the periphery of the crucible and should lead to a radial chemical gradient of Tm content due to segregation phenomenon. However, as hereafter reported, partition coefficient of Tm is very close to unity. The observable segregation phenomenon of Tm in the radial direction, with a maximum crystal radius of 0.5 cm, is substantially low compared to what can be slightly detected along the crystal axis, with a crystal length up to 9 cm, and has not been detected.

On the other hand, LIBS measurements performed in as-grown boules have shown a sudden drop of Tm content in the conical part compared to the cylindrical part where the distribution of [Tm] content evolves more steadily The poor mixing within the liquid phase as pointed out by above-mentioned numerical simulation may be responsible for this sudden change.

It is worth mentioning that for the low initial [Tm] content growth

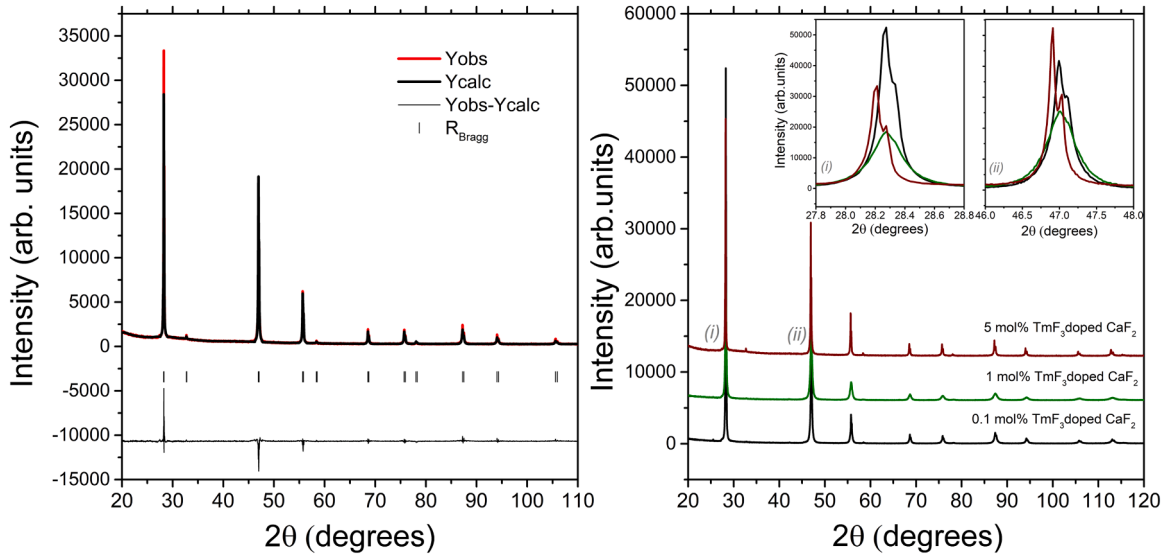

Fig. 6. (a) Calculated and measured X-Ray diffraction patterns for CaF_2 cubic structure [49] (b) X-Ray diffraction patterns for the 0.1 mol.%, 1 mol.% and 5 mol.% TmF_3-doped CaF_2 samples characteristic of the fluoride phase. (i) and (ii) Enlargements of the low-angle part of the X-ray diffraction patterns.

Table 3
Sample composition, unit cell parameters and corresponding volume for the 0.1 mol.%, 1 mol.% and 5 mol.% TmF_3 doped CaF_2 samples obtained from the Rietveld refinement for X-ray diffraction data collected on crushed single crystals.

Sample	Unit cell parameters (Å)	Volume (Å^3)	Reference
Undoped CaF_2	5.463	163.065	[49]
0.1 mol%TmF_3-doped CaF_2	5.46467(15)	163.189(8)	This work
1 mol%TmF_3-doped CaF_2	5.46619(5)	163.325(3)	This work
5 mol%TmF_3-doped CaF_2	5.47112(5)	163.768(3)	This work

attempt, with C_L^0=0.1 mol.% and C_L^0=1 mol.%, no trend in the evolution of Tm segregation along the length of the boules can be deduced, so that only boule with C_L^0=5 mol.% initial Tm content is considered. Hence, the molar error of [Tm] content in the crystal is taken as that estimated by ICP-AES (Table 2) with ±0.60 mol.%. The error of Tm content in the liquid corresponds to the accuracy of weighing TmF_3 during the crucible loading. It is about $\pm 1\times10^{-3}$ g ($\sim 4.4\times10^{-4}$ mol.%) and is neglected in the following calculations. LIBS averaged content measurements have shown a slight evolution of the [Tm] content all along the boule length with a varying [Tm] average content from 5.13 ± 0.60 mol.% to 4.57 ± 0.60 mol.% at the end of, respectively, the conical and cylindrical parts. Besides, in the seed part, [Tm] content is measured about C_S = 5.09 ± 0.60 mol.% so close to that at the end of the conical part. As shown by numerical simulation, the convection is poor in the seed location. At the liquid interface during the crystallization, Tm content supply is mainly caused by Tm diffusion and poorly by convection. The [Tm] content in the crystallized seed part may be slightly underestimated compared to what is measured in the conical part. Hence, the effective partition coefficient of [Tm] in CaF_2 is calculated with the highest value of C_S = 5.13 ± 0.60 mol.% and gives $k_{eff}([Tm])_{LIBS}$= 1.026 ± 0.120, close to unity, accordingly to what was predicted by Fedorov *et al.* [61].

3.4.2. Spectroscopic measurements

The absorption spectra of TmF_3-doped CaF_2 crystals reveal the characteristic absorption bands of both Tm^{2+} and Tm^{3+} cations (Fig. 9). The peak at 260 nm corresponding to $^3H_6 \rightarrow {}^3P_2$ transition, and the absorption band at 409 nm corresponding to the transition in between $4f^{13}(^2F_{7/2})$ ground state to the $4f^{12}5d^1$ excited state, were chosen for the determination of the effective partition coefficient of Tm^{2+} and Tm^{3+} respectively, by the optical absorption method. In Fig. 9, the $^3H_6 \rightarrow {}^3P_2$ transition at 260 nm for Tm^{3+} and the $4f^{13}(^2F_{7/2}) \rightarrow 4f^{12}5d^1$ transition at 409 nm for Tm^{2+} were selected based on their characteristic absorption features and suitability for quantitative analysis. As demonstrated recently [21], the 260 nm band of Tm^{3+} ions exhibits a linear trend of increasing the absorption coefficient with TmF_3 concentration, supporting its effective use here. To mitigate potential nonlinearity effects, such as self-absorption at higher concentrations, the stronger Tm^{2+} absorption band at 409 nm was also employed for accurate detection.

This method is based on the following two laws:

(a) according to the Beer–Lambert law the absorption coefficient, α is proportional to the sample concentration, C, $\alpha = aC$, where a is the absorption coefficient for unit dopant concentration and unit light path length. The dopant concentration of a each slice can be estimated using the equation:

$$C = \frac{\alpha}{a} = \frac{23,0258}{ad} \quad (1)$$

where d is the sample thickness in mm.

(b) The dopant concentration along the growth axis at the distance z from the origin of the crystal can be obtained by using the equation [62]:

$$C_S(z) = C_L^0 k_{eff}[1 - g(z)]^{k_{eff}-1} \quad (2)$$

where $g(z)$ is the crystallized fraction of the melt.

Therefore, the dopant distribution along the crystal length can be estimated using the optical absorption method and the effective segregation coefficient can be calculated. The absorption coefficients $\alpha(z)$ for Tm^{3+} and Tm^{2+} ions are measured from the optical absorption spectrum of every slice. Using the Eqs. (1) and (2), the following expression is obtained:

$$log\alpha(z) = (k_{eff} - 1)\log\left(1 - \frac{z}{L}\right) + \log(ak_{eff}C_L^0) \quad (3)$$

The effective partition coefficient was estimated from the slope $m = k_{eff}$ - 1, of the fitting line of log $\alpha(z)$ vs. log(1 – z/L), where 'log' denotes the decimal logarithm. The calculated effective partition coefficients are shown in Fig. 10 and Table 4, together with the results provided by other authors [55–60]. As the concentration of the TmF_3 in the initial melt increases, the effective partition coefficient, k_{eff} of both Tm^{3+} and Tm^{2+} ions decreases. This is in a good agreement with previous results reported for other rare earth-based trifluorides with close cationic radius

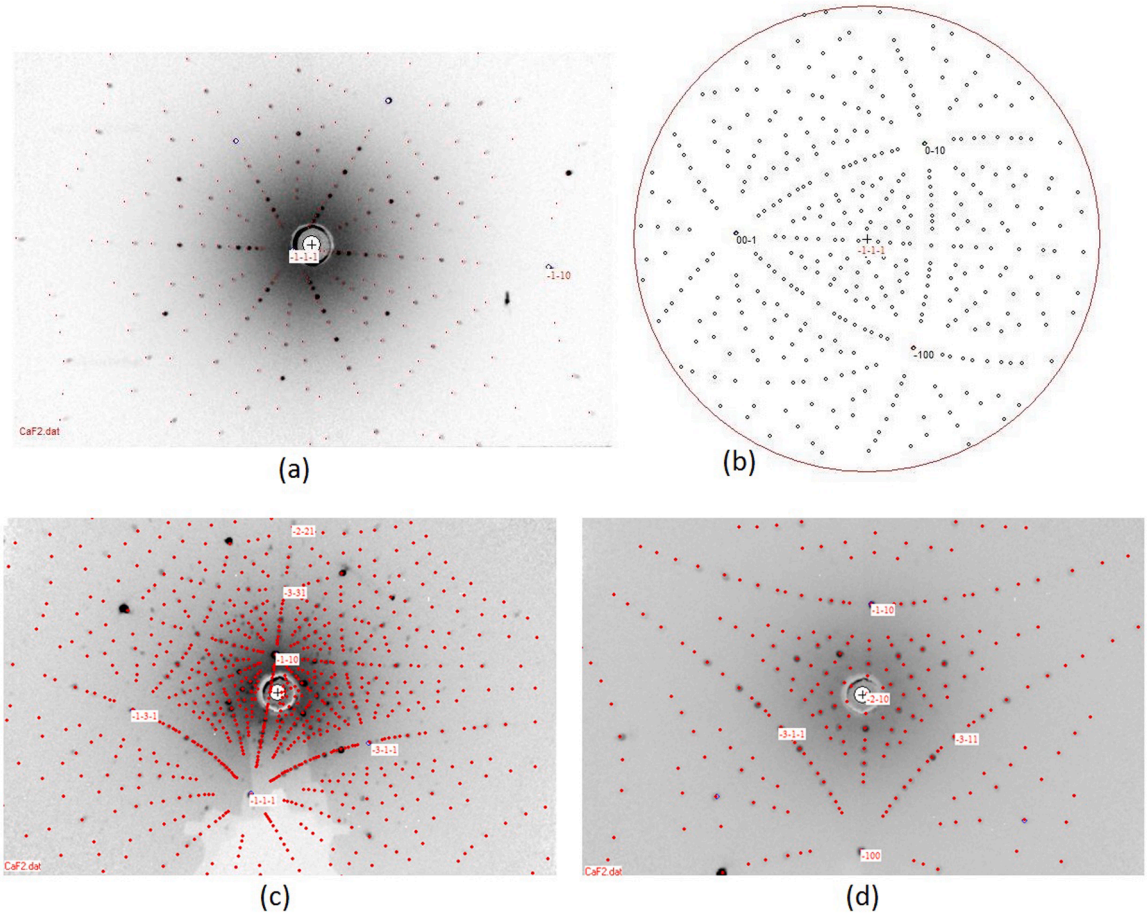

Fig. 7. Example of Laue patterns at the beginning of cylindrical part of as-grown boules. (a) Cleavage plan orientation in 5 mol.% Tm-doped CaF_2 with (b) stereographic projection. Examples of (c) natural growth direction in 0.1 mol.% Tm-doped CaF_2 and (d) natural growth direction 1 mol.% Tm-doped CaF_2. Red dots correspond to simulated Laue pattern superimposed to experimental one with black spots.

than those of Tm^{3+} or Tm^{2+} such as Er^{3+} cations [2] as well as Yb^{3+} and Yb^{2+} cations in fluorite crystals [63].

Considering the 1 mol.% and 5 mol.% TmF_3-doped CaF_2 attempts, the global partition coefficients calculated from Optical Absorption (OA) $k_{eff}([Tm])_{OA}$ (where [Tm] total content corresponds to Tm^{2+} and Tm^{3+} contents) evolve from a value higher to lower than unity. Whether both $k_{eff}(Tm^{2+})_{OA}$ and $k_{eff}(Tm^{3+})_{OA}$ are higher than one, then $k_{eff}([Tm])_{OA}$ must be higher than one, and vice versa. These results obtained from optical measurements are in good agreement with LIBS results measured on 5 mol.% TmF_3-doped CaF_2 crystal which allow a partition coefficient lower than unity with $0.906 \leq k_{eff}([Tm])_{LIBS} \leq 1.146$. From both LIBS - ICP-AES and optical absorption measurements, for 5 mol.% TmF_3-doped CaF_2, partition coefficient of Tm is estimated to be $0.906 \leq k_{eff}([Tm])_{LIBS+OA} < 1$.

3.4.3. Discussion

In analogy with Yb-doped fluorides, Tm ions may exhibit clustering behavior at higher concentrations, potentially impacting Rare Earth absorption intensities. Previous works on Yb-doped CaF_2, as reported by Nicoara *et al.* [46,64], showed that at low concentrations, the segregation coefficients for Yb^{3+} and Yb^{2+} ions were close to unity, resulting in a relatively homogeneous distribution. However, clustering increased with dopant concentration, affecting absorption characteristics. For the Tm-doped system studied here, we assume that the absorption coefficient α remains proportional to the Tm concentration for the selected transition. This assumption is consistent with the linear trend observed for Tm absorption bands in similar low-concentration fluoride hosts [21], which suggests minimal influence of clustering effects under our experimental conditions. Although clustering could introduce nonlinearity and measurement error at higher concentrations, our analysis is based on a concentration range where linearity is expected to hold, as observed in analogous systems [21,46].

- **Congruent melting point in CaF_2-TmF_3 phase diagram**

As reported by Sobolev *et al.* [65], the phase diagram CaF_2-TmF_3 does not exhibit a maximum of the liquidus curve corresponding to a congruent melting point in its CaF_2-rich region, although it should exist as previously mentioned [61]. LIBS as well as optical absorption spectroscopy measurements have shown a partition coefficient of Tm in CaF_2 higher than unity for 1 mol.% Tm initial content and lower than unity for 5 mol.% Tm initial content. That highlights a change in the slope signs of both solidus and liquidus curves in the CaF_2-TmF_3 phase diagram. Indeed, when the slope signs of both liquidus and solidus curves are positive, during the crystallization, the Tm content is always higher in the crystal than that in the liquid leading, thus to $k_{eff} > 1$. On the contrary, when the slope signs of both liquidus and solidus curves are negative, the concentration of Tm in the liquid is higher than that in the crystal leading, thus, to $k_{eff} < 1$. We conclude that the expected congruent melting point previously predicted [61,65], ranges higher than 1 mol% and below 5 mol.% TmF_3 molar fraction.

- **Carbon environment influence on Tm^{3+} reduction into Tm^{2+}**

The presence of Tm^{2+} peaks underlines the partial reduction of Tm^{3+} into Tm^{2+} during the CaF_2 growth process. The high purity of the

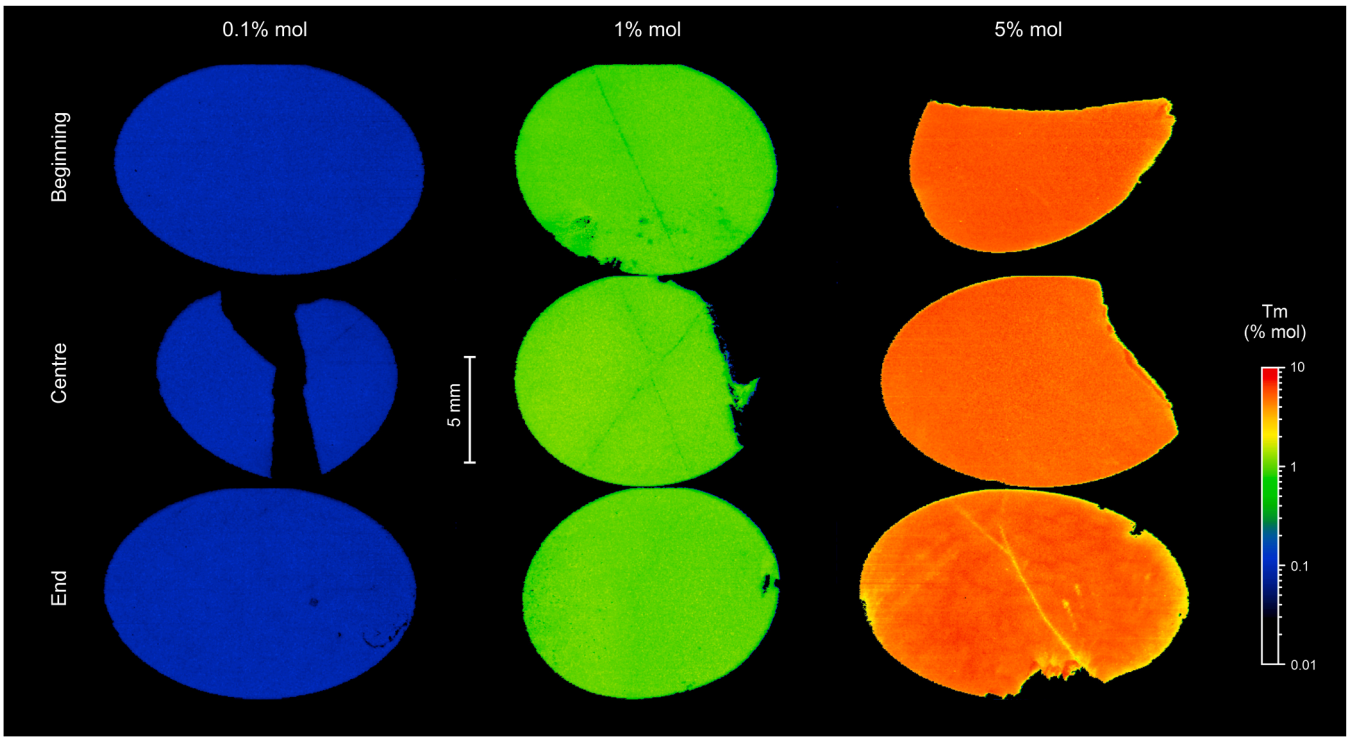

Fig. 8. LIBS imaging on three samples of each of the three attempts at different stages of the 3 boules: beginning, centre and end of the cylinder. Colours illustrate the relative concentration of Tm content with increasing Tm content from blue colour (lower content) to green colour (intermediate content) and to red colour (higher content).

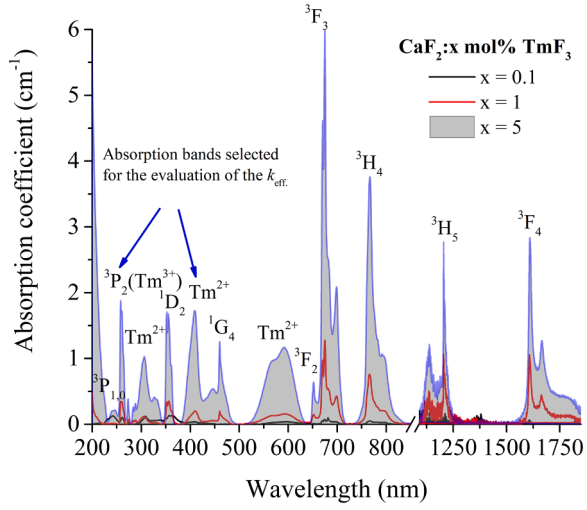

Fig. 9. Room temperature absorption spectra of TmF_3-doped CaF_2 crystals where the transitions of the observed absorption bands are depicted. The absorption bands selected for evaluating the effective partition coefficients (k_{eff}) of Tm^{2+} and Tm^{3+} are indicated with blue arrows.

commercial TmF_3 raw material used in this work is not questioned. Ellingham diagram calculations related to F_2 gas [66] is considered up to the maximum growth working temperature 1785 K. The Gibbs free enthalpies of reaction $\Delta_rG°$ of fluorides are calculated from enthalpies of formation $\Delta_fH°$ and standard entropies S°(298 K) (Table 5). Note that $\Delta_rG°(TmF_{3(l)})$ has been extrapolated beyond $TmF_{3(s)}$ melting point from $\Delta_rG°(TmF_{3(s)})$ by assuming similar $\Delta_fH°$ and S° values for both solid and liquid phases such as observed with $CaF_{2(s,l)}$. It is consistent with the values reported by Greis *et al.* [67] who mentioned the same trend for both $TmF_{3(s)}$ and $TmF_{3(l)}$. Ellingham calculations pointed out that $C_{(s)}$, $CaF_{2(s,l)}$ and $TmF_{3(s,l)}$ are the stable compounds in the present system under vacuum. However, the partial pressures of $F_{2(g)}$ have been calculated in the range 1691K-1785K for TmF_3 and CaF_2 formation equilibrium. At these temperatures, respectively, partial vapour pressure $P(F_{2(g)})$ has been estimated ranging from $\sim 1\times10^{-29}$ to 5×10^{-26} atm. for CaF_2 and $P(F_{2(g)})$ $\sim 1\times10^{-27}$ to 1×10^{-24} atm. for TmF_3. As the growth is performed under vacuum atmosphere in a $C_{(s)}$ graphite crucible, the reaction between the continuously released $F_{2(g)}$ vapour and $C_{(s)}$ can form continuously $CF_{4(g)}$. This F_2 depletion in the liquid phase leads to the Tm^{3+} to Tm^{2+} conversion driven by the charge compensation phenomenon within the melt and the as-grown crystal.

- **Tm^{3+} reduction by synproportionation reaction**

Although TmF_3 volatilization is considered as congruent [70,71], stable non-stoichiometric thulium-based fluorides such as $Tm_{13}F_{32-\delta}$ [72], $TmF_{2.37}$ [73], $TmF_{2.40}$ [67,70,74], $TmF_{2.38}$ and $TmF_{2.42}$ [75] are reported when TmF_3 is in the presence of metallic Tm. These compounds are formed by synproportionation reaction [76] and exhibit a mixed valence of Tm. They are chemically similar to other well-known rare-earth trifluorides, with a higher divalent state stability [76], that reduce to stoichiometric or non-stoichiometric compounds such as EuF_3 into EuF_2 [70], SmF_3 into SmF_2, $SmF_{2.35}$ and $SmF_{2.40}$ [70,77], and YbF_3 into YbF_2, $YbF_{2.375}$ and $YbF_{2.40}$ [70,78]. Such redox reaction for Tm can be written theoretically as $Tm + 2TmF_3 \leftrightharpoons 3TmF_2$ where a small Tm amount can be originated from the formation equilibrium of TmF_3. However, TmF_2 having a hypothetical existence [67,70,74], in the case of CaF_2:Tm^{2+}, thermodynamic instability of divalent state of Tm has been reported [76,79] causing Tm^{2+} to slowly oxidize into Tm^{3+} via the reverse redox reaction known as disproportionation reaction: $3TmF_2 \leftrightharpoons Tm + 2TmF_3$. Hence, the qualitative but significant spectroscopic detection of both Tm^{2+} and Tm^{3+} in as-grown CaF_2 single crystal of the present work is assumed to arise partially from the synproportionation reaction of TmF_3.

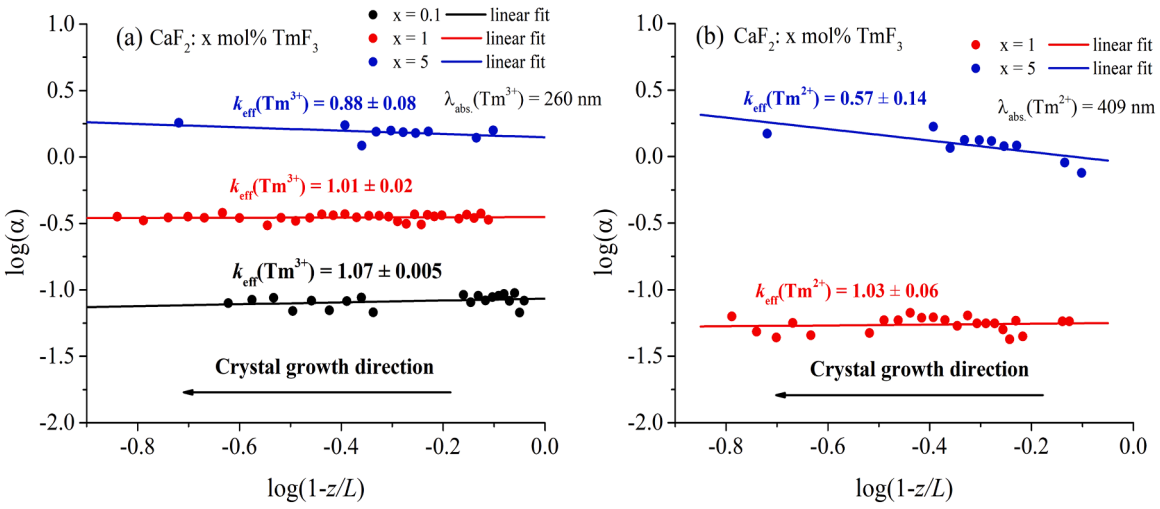

Fig. 10. partition coefficients of (a) Tm^3 cations and (b) Tm^{2+} cations in TmF_3: doped CaF_2 crystals. Due to inaccuracy of measurements and the very low Tm2+ content for x=0.1 %, no line could be fitted with experimental data.

Table 4
Calculated effective segregation coefficient of CaF_2: x mol% TmF_3 crystals (x = 0.1 %, 1 % and 5 %).

Ions	x = 0.1 This work	x = 1 This work	x = 5 This work	Tm: YAG Crystal [57]	Tm: Ca(Gd,Lu)AlO_4 crystal [55]	Tm: YAP [58]	Tm: Fe-garnet crystal [60]	Tm: $Ca_3(VO4)_2$ [59]	Tm: CGA [56]
Tm^{3+}	1.070 ± 0.005	1.01 ± 0.02	0.88 ± 0.08	1.04	0.90	0.88	0.85	0.8	0.61
Tm^{2+}	-	1.03 ± 0.06	0.57 ± 0.14	-	-	-	-	-	-

Table 5
Thermodynamics values of C, Ca and Tm fluorides used in Ellingham diagram.

Element or compound (s=solid, l=liquid, g=gas)	$\Delta_f H^0$ (kJ.mol^{-1})	S^0 (J.K^{-1}.mol^{-1})	Melting or boiling point (K)	Chemical equilibrium	ΔrH^0 (kJ.mol^{-1})	ΔrS^0 (J.K^{-1}.mol^{-1})	Reference
F_2 (g)	0	202.80	53.33	X	X	X	[66–69]
C (s)	0	5.74	3823	X	X	X	
CF_4 (g)	−933.60	261.60	89.4	½ C(s) + F_2(g) ⇋ ½ CF_4(g)	−466.8	−74.87	
Ca (s)	0	41.59	1115	X	X	X	
Ca (l)	7.79	45.51	1757	X	X	X	
Ca (g)	177.80	154.89	X	X	X	X	
CaF_2 (s)	−1228	68.50	1691	Ca(s) + F_2(g) ⇋ CaF_2(s)	−1228.00	−175.89	
CaF_2 (s)	"	"	"	Ca(l) + F_2(g) ⇋ CaF_2(s)	−1235.79	−179.81	
CaF_2 (l)	−1184.07	92.59	1757	Ca(l) + F_2(g) ⇋ CaF_2(l)	−1191.86	−155,72	
CaF_2 (l)	"	"	"	Ca(g) + F_2(g) ⇋ CaF_2(l)	−1361.87	−265.097	
Tm (s)	0	74	1818	X	X	X	
TmF_3 (s,l)	−1695	118	1431	⅔ Tm(s) + F_2(g) ⇋ ⅔ TmF_3(s,l)	−1130.00	−173.47	

4. Conclusion

Centimetre-sized Tm-doped CaF_2 crystals were successfully grown by the Bridgman-Stockbarger technique with different TmF_3 initial contents: 0.1 mol.%, 1 mol.% and 5 mol.%. CaF_2 crystal habit was highlighted by Laue diffraction which have shown that natural growth orientation is preferentially along the (110) and (210) crystallographic directions with G=12 $K.cm^{-1}$ as thermal gradient and v=4 $mm.h^{-1}$ as pulling speed. A drop of global [Tm] content in the conical part of the as-grown boule was highlighted by LIBS measurements. As suggested by numerical modelling, it is caused by a poor mixing of elements in the liquid phase at the beginning of the growth due to an one order of magnitude lower convection in comparison with the melt convection in the later growth stages, where the bending of solid-liquid interface generates a higher convection. Chemical characterization has shown that single crystals exhibit a highly homogenous [Tm] content distribution throughout the whole boule volume but optical absorption measurements have displayed the presence of both Tm^{3+} and Tm^{2+} cations. The simultaneous presence of these cations is assumed to be likely due to the carbon environment and synproportionation partial reaction of TmF_3 which leads to Tm-mixed-valency-doped CaF_2 single crystals since Tm^{2+} can enter easily in the CaF_2 matrix because no charge compensation is needed.

Through the results from growth attempt with C_L^0=5 mol.% TmF_3 initial content, effective partition coefficient of [Tm] has been estimated. LIBS coupled with ICP-AES gave $0.906 < k_{eff}([Tm])_{LIBS} < 1.126$ where [Tm] total content corresponds to both Tm^{2+} and Tm^{3+} contents. Furthermore, optical absorption measurements gave $k_{eff}(Tm^{3+})_{OA} = 0.88 \pm 0.08$ and $k_{eff}(Tm^{2+})_{OA}=0.52 \pm 0.14$ leading to a global partition coefficient $k_{eff}([Tm])_{OA} <1$. From these results, it is finally concluded that $0.906 \leq k_{eff}([Tm])_{LIBS+OA} < 1$ suggesting, thus, that the expected congruent point in the CaF_2-rich region of CaF_2-TmF_3 phase diagram does exist and lie within a range higher than 1 mol.% and lower than 5 mol.% TmF_3 molar fraction. Further physical characterization of Tm^{2+}

and Tm^{3+} content, such as with Electron Paramagnetic Resonance (EPR) technique and X-ray Photoelectron Spectroscopy (XPS), should have to be carried out in order to quantify their amount in both the raw material and as-grown crystals.

CRediT authorship contribution statement

Frédéric Pelascini: Writing – original draft, Resources, Formal analysis, Data curation. **Daniel Vizman:** Writing – original draft, Software, Methodology, Investigation, Formal analysis, Data curation. **Jérôme Debray:** Writing – original draft, Resources, Investigation, Formal analysis, Data curation. **Vincent Motto-Ros:** Writing – original draft, Resources, Investigation, Formal analysis, Data curation. **Dragos Tatomirescu:** Writing – original draft, Software, Investigation, Formal analysis, Data curation. **Alexandra Popescu:** Writing – original draft, Software, Methodology, Investigation, Formal analysis, Data curation. **Maria Poienar:** Writing – original draft, Software, Investigation, Formal analysis, Data curation. **Carla Schornig:** Writing – original draft, Methodology, Investigation, Formal analysis, Data curation. **Marius Stef:** Writing – original draft, Methodology, Investigation, Formal analysis, Data curation. **Philippe Roger Veber:** Writing – original draft, Validation, Supervision, Resources, Project administration, Methodology, Investigation, Funding acquisition, Formal analysis, Data curation. **Gabriel Buse:** Writing – original draft, Resources, Investigation, Formal analysis, Data curation.

Declaration of Competing Interest

The authors declare the following financial interests/personal relationships which may be considered as potential competing interests: Philippe Veber reports financial support was provided by European Commission. Philippe Veber reports a relationship with European Commission that includes: funding grants. If there are other authors, they declare that they have no known competing financial interests or personal relationships that could have appeared to influence the work reported in this paper.

Acknowledgement

This work is funded by European Commission within the framework of the National Recovery and Resilience Plan (PNRR) through the ESCARGOT project entitled “Enhanced Single Crystal Applications and Research in the Growth of new Optical rare earth-based compounds for sustainable and efficient Technologies” (n°: 760080/23.05.2023). The authors would like to acknowledge the Centre de diffractométrie Henri Longchambon (CDHL) in Villeurbanne for XRD measurements on crushed single crystals.

Appendix A. Supporting information

Supplementary data associated with this article can be found in the online version at doi:10.1016/j.jallcom.2024.177784.

Data availability

Data will be made available on request.

References

[1] N. Sarukura, T. Nawata, H. Ishibashi, M. Ishii, T. Fukuda, Czochralski growth of oxides and fluorides, Vol. 2 (Handbook of Crystal Growth: Bulk Crystal Growth, second ed. (2015).
[2] I. Nicoara, M. Stef, G. Buse, A. Racu, Growth and characterization of ErF3 doped BaF2 crystals, J. Cryst. Growth 547 (2020).
[3] D. Nicoară, I. Nicoară, An improved Bridgman-Stockbarger crystal-growth system, Mater. Sci. Eng. 102 (1988) L1.
[4] M. Stef, I. Nicoara, G. Buse, Spectroscopic properties of gamma irradiated CeF3 doped BaF2 crystals, AIP Conf. Proc. 2218 (2020) 040002.
[5] D.N. Karimov, I.I. Buchinskaya, Growth of KR3F10 (R = Tb–Er) crystals by the vertical directional crystallization technique. i: optimization of the melt composition for the growth of KTb3F10 and correction of the phase diagram of the KF–TbF3 system, Crystallogr. Rep. 66 (2021) 535.
[6] B. Chai, J. Lefaucheur, A.-T. Pham, G.B. Loutts, J.F. Nicholls, Growth of High-quality Single Crystals of KYF4 by TSSG Method, in Growth, Characterization, and Applications of Laser Host and Nonlinear Crystals II (SPIE), in: edited by B. Chai, 1863, 1993, pp. 131–135 (SPIE).
[7] P.W. Metz, D.-T. Marzahl, G. Huber, C. Kränkel, Performance and wavelength tuning of green emitting terbium lasers, Opt. Express 25 (2017) 5716.
[8] P.W. Metz, D.T. Marzahl, A. Majid, C. Kränkel, G. Huber, Efficient continuous wave laser operation of tb3+-doped fluoride crystals in the green and yellow spectral regions, Laser Photonics Rev. 10 (2016) 335.
[9] D. Wang, P. Lu, L. Fang, X. Zhou, J. Zhang, H. Xia, H. Song, B. Chen, Growth of KAlF4 and Na5Al3F14 aluminium fluoride single crystals by Bridgman method, Cryst. Res. Technol. (2022) 2200013.
[10] S. Kalusniak, E. Castellano-Hernández, H. Yalçinoğlu, H. Tanaka, C. Kränkel, Spectroscopic properties of Tb3+ as aN Ion for Visible Lasers, Appl. Phys. B Lasers Opt. 128 (2022) 32.
[11] D.N. Karimov, I.I. Buchinskaya, N.A. Arkharova, A.G. Ivanova, A.G. Savelyev, N. I. Sorokin, P.A. Popov, Growth peculiarities and properties of KR3F10 (R = Y, Tb) single crystals, Crystals 11 (2021) 285.
[12] P. Loiko, J. Doualan, L. Guillemot, R. Moncorge, A. Benayad, E. Dunina, A. Kornienko, L. Fomicheva, A. Braud, P. Camy, Emission properties of Tm3+-doped CaF2, KY3F10, LiYF4, LiLuF 4 and BaY2F8 crystals at 1.5 Mm and 2.3 Mm, J. Lumin. 225 (2020) 117279.
[13] H. Chen, H. Uehara, H. Kawase, R. Yasuhara, Efficient visible laser operation of Tb: LiYF 4 and LiTbF4, Opt. Express 28 (2020) 10951.
[14] S.L. Baldochi, I.M. Ranieri, A short review on fluoride laser crystals grown by Czochralski method at IPEN, Acta Phys. Pol. A 124 (2013) 286.
[15] H. Li, J. Wang, J. Chen, Y. Dai, L. Su, X. Li, A.M. Kalashnikova, A. Wu, Bridgman growth and magneto-optical properties of CeF3 crystal as Faraday rotator, Opt. Mater. 100 (2020) 109675.
[16] P. Pues, F. Baur, S. Schwung, D. Rytz, R. Pöttgen, C. Paulsen, O. Janka, B. Rendenbach, D. Johrendt, T. Jüstel, Temperature and time-dependent luminescence of single crystals of KTb3F10, J. Lumin. 227 (2020) 117523.
[17] A. Yoshikawa, K. Kamada, M. Nikl, K. Aoki, H. Sato, J. Pejchal, T. Fukuda, Growth and luminescent properties of Pr:KY3F10 single crystal, J. Cryst. Growth 285 (2005) 445.
[18] L. Guillemot, P. Loiko, R. Soulard, A. Braud, J.-L. Doualan, A. Hideur, P. Camy, Close look on cubic Tm:KY3F10 crystal for highly efficient lasing on the 3H4 → 3H5 transition, Opt. Express 28 (2020) 3451.
[19] Z. Zhang, X. Guo, J. Wang, C. Zhang, J. Liu, L. Su, High-efficiency 2micrometer continuous-wave laser in laser diode-pumped Tm3+, La3+: CaF2 single crystal, Opt. Lett. 43 (2018) 4300.
[20] Y. Wang, S. Wang, J. Wang, Z. Zhang, Z. Zhang, R. Liu, Y. Zu, J. Liu, L. Su, High-efficiency ~2 Mm CW laser operation of LD-pumped Tm 3+:CaF 2 SIngle-crystal Fibers, Opt. Express 28 (2020) 6684.
[21] C. Schornig, M. Stef, G. Buse, M. Poienar, P. Veber, D. Vizman, Spectroscopic properties of TmF3-doped CaF2 crystals, Materials 17 (2024) 4965.
[22] J.L. Benak, T.B. Selover, Wettability of graphite by barium fluoride calcium fluoride eutectic, *Carbon* 6 (1968) 229.
[23] L. Su, Y. Dong, W. Yang, T. Sun, Q. Wang, J. Xu, G. Zhao, Growth, characterization and optical quality of caf2 single crystals grown by the temperature gradient technique, Mater. Res. Bull. 40 (2005) 619.
[24] J.M. Ko, S. Tozawa, A. Yoshikawa, K. Inaba, T. Shishido, T. Oba, Y. Oyama, T. Kuwabara, T. Fukuda, Czochralski growth of UV-grade CaF2 single crystals using ZnF2 additive as scavenger, J. Cryst. Growth 222 (2001) 243.
[25] M. Kurz, G. Müller, Control of thermal conditions during crystal growth by inverse modeling, J. Cryst. Growth 208 (2000) 341.
[26] M. Kurz, A. Pusztai, G. Müller, Development of a new powerful computer code CrysVUN + + especially designed for fast simulation of bulk crystal growth processes, J. Cryst. Growth 198–199 (1999) 101.
[27] J. Fainberg, D. Vizman, J. Friedrich, G. Mueller, A new hybrid method for the global modeling of convection in CZ crystal growth configurations, J. Cryst. Growth 303 (2007) 124.
[28] X. Li, D. Jiang, J. Wang, X. Qian, R. Liu, Q. Wu, Z. Zhang, L. Su, Numerical simulation of heat transfer and convection for CaF2 crystal growth by vertical Bridgman growth method, Cryst. Res. Technol. 55 (2020) 1900191.
[29] S. Andersson, G. Backstrom, Thermal conductivity and heat capacity of single-crystal LiF and CaF2 under hydrostatic pressure, J. Phys. C Solid State Phys. 20 (1987) 5951.
[30] D.R. Huffman, M.H. Norwood, Specific heat and elastic constants of calcium fluoride at low temperatures, Phys. Rev. 117 (1960) 709.
[31] CRYSTRAN, Crystran- Calcium Fluoride (CaF2) Data Sheet, ⟨https://www.crystran.com/optical-materials/calcium-fluoride-caf2⟩.
[32] X. Chen, S. Jinguu, S. Nishimura, Y. Oyama, K. Terashima, Density and surface tension of molten calcium fluoride, J. Cryst. Growth 240 (2002) 445.
[33] Y. Da-Lun, H. Jianhua, The Handbook of Thermodynamic Data for Practical Inorganic Compounds, Metallurgical Industry Press, Beijing, 2002.
[34] O. Takeda, Y. Hoshino, Y. Anbo, K. ichi Yanagase, M. Aono, Y. Sato, Viscosity oF Molten Alkaline-earth Fluorides, Int. J. Thermophys. 36 (2015) 648.
[35] B. Barvinschi, P. Barvinschi, Numerical investigation of crystal growth in a vertical Bridgman configuration using a mushy region model, J. Optoelectron. Adv. Mater. 17 (2015) 431.

[36] H. Chu, F. Liu, H. Zhou, Calculations of gas thermal radiation transfer in one-dimensional planar enclosure using LBL and SNB Models, Int. J. Heat. Mass Transf. 54 (2011) 4736.
[37] V. Kez, J.L. Consalvi, F. Liu, J. Ströhle, B. Epple, Assessment of several gas radiation models for radiative heat transfer calculations in a three-dimensional oxy-fuel furnace under coal-fired conditions, Int. J. Therm. Sci. 120 (2017) 289.
[38] P. Villars and K. Cenzual, editors, CaF2 Crystal Structure: Datasheet from PAULING FILE Multinaries Edition – 2022, in: SpringerMaterials (Dataset ID: Sd_0553631).
[39] J. Rodriguez-Carvajal, FULLPROF: A Program for Rietveld Refinement and Pattern Matching Analysis, in: : Proceedings of the Satellite Meeting on Powder Diffraction of the XV Congress of the IUCr, Toulouse, France,127 (1990).
[40] B. Ouladdiaf, J. Archer, G.J. McIntyre, A.W. Hewat, D. Brau, S. York, OrientExpress: a new system for laue neutron diffraction, Phys. B Condens. Matter 385–386 (2006) 1052.
[41] V. Motto-Ros, S. Moncayo, C. Fabre, B. Busser, in: J.P. Singh, S. Thakur (Eds.), Chapter 14 - LIBS Imaging Applications, Elsevier, Amsterdam, 2020, pp. 329–346.
[42] C. Fabre, D. Devismes, S. Moncayo, F. Pelascini, F. Trichard, A. Lecomte, B. Bousquet, J. Cauzid, V. Motto-Ros, Elemental imaging by laser-induced breakdown spectroscopy for the geological characterization of minerals, J. Anal. At. Spectrom. 33 (2018) 1345.
[43] L. Sancey, V. Motto-Ros, B. Busser, S. Kotb, J.M. Benoit, A. Piednoir, F. Lux, O. Tillement, G. Panczer, J. Yu, Laser spectrometry for multi-elemental imaging of biological tissues, Sci. Rep. 4 (2014) 6065.
[44] J.O. Cáceres, F. Pelascini, S. Moncayo, F. Trichard, G. Panczer, A. Marín-Roldán, J. A. Cruz, I. Coronado, J. Martín-Chivelet, Megapixel multi-elemental imaging by laser-induced breakdown spectroscopy, a technology with considerable potential for paleoclimate studies, Sci. Rep. 7 (2017) 5080.
[45] I. Nicoara and M. Stef, Growth and Characterization of Doped CaF2 Crystals, in Modern Aspects of Bulk Crystal and Thin Film Preparation, edited by N. Kolesnikov and E. Borisenko, Vol. chapter 4 (2012), 71–96.
[46] I. Nicoara, G. Buse, M. Bunoiu, Segregation Coefficient of Yb3+ and Yb2+ Ions in YbF3 Doped BaF2 Crystals, AIP Conf. Proc. 1634 (2014) 111–114.
[47] F. Barvinschi, O. Bunoiu, I. Nicoara, D. Nicoara, J.L. Santailler, T. Duffar, Factors affecting the isotherm shape of semi-transparent BaF2 crystals grown by Bridgman method, J. Cryst. Growth 237–239 (2002) 1762.
[48] F. Barvinschi, I. Nicoara, J.L. Santailler, T. Duffar, Pseudo-transient heat transfer in vertical Bridgman crystal growth of semi-transparent materials, Model. Simul. Mater. Sci. Eng. 6 (1998) 691.
[49] M. Schreyer, L. Guo, S. Thirunahari, F. Gao, M. Garland, Simultaneous determination of several crystal structures from powder mixtures: the combination of powder X-ray diffraction, band-target entropy minimization and Rietveld methods, J. Appl. Crystallogr. 47 (2014) 659.
[50] N. Senguttuvan, M. Aoshima, K. Sumiya, H. Ishibashi, Oriented growth of large size calcium fluoride single crystals for optical lithography, J. Cryst. Growth 280 (2005) 462.
[51] W.A. Tiller, K.A. Jackson, J.W. Rutter, B. Chalmers, The redistribution of solute atoms during the solidification of metals, Acta Met. 1 (1953) 428.
[52] W.W. Mullins, R.F. Sekerka, Stability of a planar interface during solidification of a dilute binary alloy, J. Appl. Phys. 35 (1964) 444.
[53] R.F. Sekerka, Morphological stability, J. Cryst. Growth 3–4 (1968) 71.
[54] P.P. Fedorov, et al., Morphological stability of the solid–liquid interface during melt crystallization of Ca1–XSrxF2 Solid Solution, Crystallogr. Rep. 63 (2018) 837.
[55] Z. Pan, et al., Tm,Ho:Ca(Gd,Lu)AlO4 crystals: crystal growth, structure refinement and Judd-Ofelt analysis, J. Lumin. 246 (2022) 1.
[56] J. Di, X. Xu, C. Xia, Q. Sai, D. Zhou, Z. Lv, J. Xu, Growth and spectra properties of Tm, Ho doped and Tm, Ho co-doped CaGdAlO4 crystals, J. Lumin. 155 (2014) 101.
[57] P. Song, Z. Zhao, X. Xu, B. Jang, P. Deng, J. Xu, Growth and properties of Tm: YAG crystals, J. Cryst. Growth 270 (2004) 433.
[58] Y. Lu, J. Wang, Y. Yang, Y. Dai, A. Dong, B. Sun, Growth and optical properties of Tm:YAlO3 single crystals with different Tm concentrations, J. Alloy. Compd. 429 (2007) 296.
[59] L.I. Ivleva, E.E. Dunaeva, I.S. Voronina, M.E. Doroshenko, A.G. Papashvili, Ca3 (VO4)2:Tm3+ — a new crystalline medium for 2-Mm lasers, J. Cryst. Growth 501 (2018) 18.
[60] V.I. Chani, G. Boulon, W. Zhao, T. Yanagida, A. Yoshikawa, Correlation between segregation of rare earth dopants in melt crystal growth and ceramic processing for optical applications, Jpn. J. Appl. Phys. 49 (2010) 075601.
[61] P.P. Fedorov, B.P. Sobolev, Phase diagrams of the CaF2-(Y, Ln)F3 systems: II. A discussion, J. Less Common Met. 63 (1979) 31.
[62] M. Paraschiva, I. Nicoara, M. Stef, O.M. Bunoiu, Distribution of Pb2+ ions in PbF2-doped CaF2 Crystals, Acta Phys. Pol. A 117 (2010) 466.
[63] M. Stef, I. Nicoara, D. Vizman, Distribution of Yb3+ and Yb2+ ions along YbF3-doped BaF2 crystals, Cryst. Res. Technol. 53 (2018) 1.
[64] I. Nicoara, L. Lighezan, M. Enculescu, I. Enculescu, Optical spectroscopy of Yb2+ ions in YbF3-doped CaF2 crystals, J. Cryst. Growth 310 (2008) 2026.
[65] B.P. Sobolev, P.P. Fedorov, Phase diagrams of the CaF2-(Y, Ln)F3 systems: I. experimental, J. Less Common Met. 60 (1978) 33.
[66] T.B. Reed, J. Klerer, Free energy of formation of binary compounds: an Atlas of charts for high-temperature chemical calculations, J. Electrochem. Soc. 119 (1972) 329Ca.
[67] O. Greis and J.M. Haschke, Chapter 45: Rare earth fluorides, in: Handbook on the Physics and Chemistry of Rare Earths, Edited by K.A. Gschneidner, Jr. and L. Eyring, 5 (1982), 387–460.
[68] M.W. Chase, NIST-JANAF Thermochemical Tables, 4th Ed. J. Phys. Chem. Ref. Data, 9 **1** & **2**, 3, J. Phys. Chem. Ref. Data Monogr. (1998), 9 **1** & **2**, 3.
[69] W.M. Haynes, D.R. Lide, T.J. Bruno. CRC Handbook of Chemistry and Physics, ninety seveth ed., CRC Press, Boca Raton, Florida, 2016.
[70] H.A. Eick, H. Luke, C.G. Biefeld, R.M. Biefeld, B.L. Clink, and J.T. Richards, An Investigation of Some Lanthanide Carbon, Nitrogen, Chalcogen and Halogen Systems at Elevated Temperatures - Michigan State University, Progress Report N° COO-716-08, 1975.
[71] R.M. Biefeld, H.A. Eick, Vaporization system reactions in the thulium-fluorine, J. Less Commom Met. 45 (1976) 117.
[72] O. Greis, T. Petzel, Darstellung Und Eigenschaften von Tm13F32 - δ, Z. Anorg. Allg. Chem. - J. Inorg. Gen. Chem. 434 (1977) 89.
[73] K.A. Gschneidner and L. Eyring, Handbook on the Physics and Chemistry of Rare Earths, Non-Metallic Compounds – II, Vol. 4, North Holland Publishing Company, 1979).
[74] B.G. Müller, Lanthanide Fluorides, Volume 2, in: G. Meyer, L. Morss (Eds.), Synthesis of Lanthanide and Actinide Compounds, Springer, 1991, p. 55.
[75] A.P. Ivanenko, N.M. Kompanichenko, A.A. Omelchuk, V.F. Zinchenko, E. V. Timukhin, Synthesis and optical properties of non-stoichiometric lanthanide (Sm, Eu, Tm, Yb) fluorides, Russ. J. Inorg. Chem. 55 (2010) 841.
[76] G. Meyer, Reduced halides of the rare-earth elements, Chem. Rev. 88 (1988) 93.
[77] J.J. Stezowski, H.A. Eick, Nonstoichiometry in the Samarium (II) fluoride-samarium (III) fluoride system, Inorg. Chem. 179 (1969) 1102.
[78] T. Petzel, O. Greis, The vaporization behavior of ytterbium(III) fluoride and ytterbium(II) fluoride, J. Less Common Met. 46 (1976) 197.
[79] M.P. Plokker, Unfolding the Excited States Dynamics of Tm 2+-Doped Halides In Prospect of Novel Luminescence Solar Concentrators, 2021.